nuclear fusion
IAEA

PAPER • OPEN ACCESS

High erosion and re-deposition rates of tungsten in the highly collisional plasmas of Magnum-PSI

To cite this article: Mark J.H. Cornelissen *et al* 2025 *Nucl. Fusion* **65** 026008

OPEN ACCESS
IOP Publishing | International Atomic Energy Agency
Nuclear Fusion
Nucl. Fusion **65** (2025) 026008 (15pp)
https://doi.org/10.1088/1741-4326/ad97cb

High erosion and re-deposition rates of tungsten in the highly collisional plasmas of Magnum-PSI

Mark J.H. Cornelissen[1,2,*], Beata Tyburska-Pueschel[2], Marcin Rasinski[3], Serge Brons[2], Erwin Zoethout[2], Daniel Dorow-Gerspach[3], Sebastijan Brezinsek[3], Marius Wirtz[3], Gerald Pintsuk[3], Job Beckers[1] and Thomas W. Morgan[1,2]

[1] Department of Applied Physics, Eindhoven University of Technology, P.O. Box 513, Eindhoven, 5600 MB, Netherlands
[2] DIFFER—Dutch Institute for Fundamental Energy Research, De Zaale 20, Eindhoven, 5612 AJ, Netherlands
[3] Forschungszentrum Jülich GmbH, Institut für Energie- und Klimaforschung-Plasmaphysik, Jülich 52425, Germany

E-mail: m.j.h.cornelissen@tue.nl

Received 20 June 2024, revised 21 October 2024
Accepted for publication 27 November 2024
Published 23 December 2024

Abstract

Prompt re-deposition strongly reduces the migration of eroded material in current fusion devices, thus lowering core dilution and extending the lifetime of the plasma-facing components. However, under the high-density ($n_e > 2 \times 10^{20}$ m^{-3}), low-temperature ($T_e < 5$ eV) divertor plasma conditions anticipated for future fusion devices like ITER, Coulomb collisions become highly efficient. These collisions not only prevent the ions from completing their Larmor orbits but also strongly couple the sputtered impurities to the plasma, leading to impurity entrainment. Entrainment drags impurities with the plasma flow to the surface, leading to enhanced impurity impact energies as discussed in the companion paper (Cornelissen M.J.H. *et al* 2025 *Nucl. Fusion* **65** 026009), and the re-deposition of sputtered particles. This entrained re-deposition was studied with the linear plasma generator Magnum-PSI, whose linear geometry allowed for a clear distinction between entrained and prompt re-deposition. Five W targets were exposed to high-density ($n_e \approx 5 \times 10^{20}$ m^{-3}), low-temperature ($T_e \approx 1.2$ eV) argon (Ar) plasmas. The deposition pattern of tungsten (W) on molybdenum (Mo) witness plates was determined using ion beam analysis and electron scanning microscopy. As the ion-impact energy of Ar^+ increased from $E_i \approx 43$ eV to $E_i \approx 94$ eV, the local re-deposition rate decreased from $R \approx 93\%$ to $R \approx 68\%$. Entrained re-deposition became evident from an up-downstream asymmetry in the re-deposition profile and was dominant over prompt re-deposition for the exposures investigated. Although the ionization length was long, high re-deposition rates were found, revealing that neutral-ion interactions were important. Thus, entrainment will be a crucial ingredient in the erosion and re-deposition studies of future fusion reactors.

* Author to whom any correspondence should be addressed.

Supplementary material for this article is available online

Keywords: entrainment, re-deposition, tungsten, impurities, ion beam analysis, Magnum-PSI, ITER divertor

(Some figures may appear in colour only in the online journal)

1. Introduction

A major challenge in the development of fusion power is the erosion of the plasma-facing components. Erosion not only limits the divertor's lifespan but also heavily impacts the fusion power output and plasma stability. Tungsten (W) has been chosen as the plasma-facing material for ITER due to its favorable mechanical and thermal properties, which are essential to withstand extreme heat and particle fluxes [1]. However, due to the high-Z number of W, only minimal concentrations of W (<0.1%) are allowed in the plasma core before excessive radiative cooling occurs [2]. To minimize the migration of W towards the plasma core and prolong the lifetime of the divertor, it is essential to both minimize W erosion and maximize its re-deposition. Re-deposition falls into two categories: local re-deposition, where eroded material settles within the plasma-exposed area, and shadowed re-deposition, which leads to layer growth and co-deposition of hydrogen isotope ions outside of the plasma-exposed region [3]. Thus, understanding the migration of sputtered W is crucial.

In contrast to current fusion devices, the divertor plasma of ITER [4, 5], and future fusion reactors such as DEMO [6], are expected to operate under high-density ($n_e > 2 \times 10^{20}$ m^{-3}) and low-temperature ($T_e < 5$ eV) near-surface plasma conditions. In this plasma regime, Coulomb collisions become highly efficient [7]. Additionally, pronounced neutral–plasma coupling emerges in the near-surface plasma region [8]. These collisional forces lead to the entrainment of both neutral and ionized impurities. Entrainment refers to the drag on impurities by the plasma flow, leading to their acceleration towards the plasma flow velocity. Entrainment has a dual impact: on the one hand, entrainment increases the impact energies of the impurities, amplifying erosion as discussed in the companion paper [9], while on the other hand, entrainment drags sputtered impurities back to the surface, promoting W re-deposition, which will be the focus of this work. We term re-deposition by entrainment as 'entrained re-deposition' to differentiate it from prompt re-deposition, which occurs when the gyro-orbit of an ionized sputtered particle intersects with the material surface [10]. The two re-deposition mechanisms are schematically depicted in figure 1.

The erosion and re-deposition of W have been explored in various tokamaks, including JET [11], ASDEX [12, 13], and DIII-D [14]. Nevertheless, these experiments were performed under higher temperatures and lower densities than those expected in the near-surface region of ITER, resulting in a regime in which prompt re-deposition prevailed. ERO simulations have shown that friction between impurities and the background plasma heavily influences W erosion and re-deposition for high-density low-temperature plasmas [7, 15], but experimental verification is lacking. Even though the electron temperatures are low, impurities can still acquire sufficient impact energies to sputter W by their entrainment in hydrogen isotope plasmas as discussed in the companion paper [9]. In this study, the linear plasma generator Magnum-PSI [16, 17] provided a unique opportunity to study the erosion and re-deposition of W for highly collisional argon (Ar) plasmas.

To achieve a high sputtering rate, we opted for biased W targets exposed to Ar plasmas. Although this scenario differs from the D:T fusion power operation phase of ITER with impurity seeding [18] (no bias, 95% D + T, 4% He, and 1% Ne), the pure Ar plasma allows us to study the erosion and re-deposition for relevant high-density, low-temperature divertor plasma conditions without the necessity of extremely long exposures (>100 h) to reach similar erosion levels as for ITER with an impurity mixture. In addition, the impact of entrainment on W impurity transport is amplified by choosing Ar instead of ITER's impurity mixture, allowing for a better comparison to the theoretical framework. The aim of this study is twofold: to study the re-deposition of W for highly collisional plasmas, and to investigate the effect of the ion-impact energy on the re-deposition rate. The latter is closely coupled to the companion paper, whose findings reveal a large enhancement of the ion-impact energy by entrainment [9].

To achieve these goals, first, a theoretical expectation is sketched for the contribution of both re-deposition mechanisms to the total re-deposition rate. These expectations are compared to experiments in Magnum-PSI. In these experiments, a novel target design was utilized to study W deposition in close vicinity to the W source. Small W targets were biased and surrounded by floating molybdenum (Mo) witness plates to promote W erosion whilst allowing for the examination of the deposition of W on witness plates positioned within the plasma-exposed region. Net erosion of the W target was monitored using micro-trenches cut by a Focused Ion Beam (FIB) pre-exposure and by assessing mass loss. In addition, the surface morphology of the W targets was analyzed pre- and post-exposure. Lastly, we outline the anticipated role of entrained re-deposition during ITER's operational phase.

2. Theory

For the description of the two main re-deposition mechanisms, we consider the impurities as non-perturbing concerning the general description of the near-surface plasma region. This

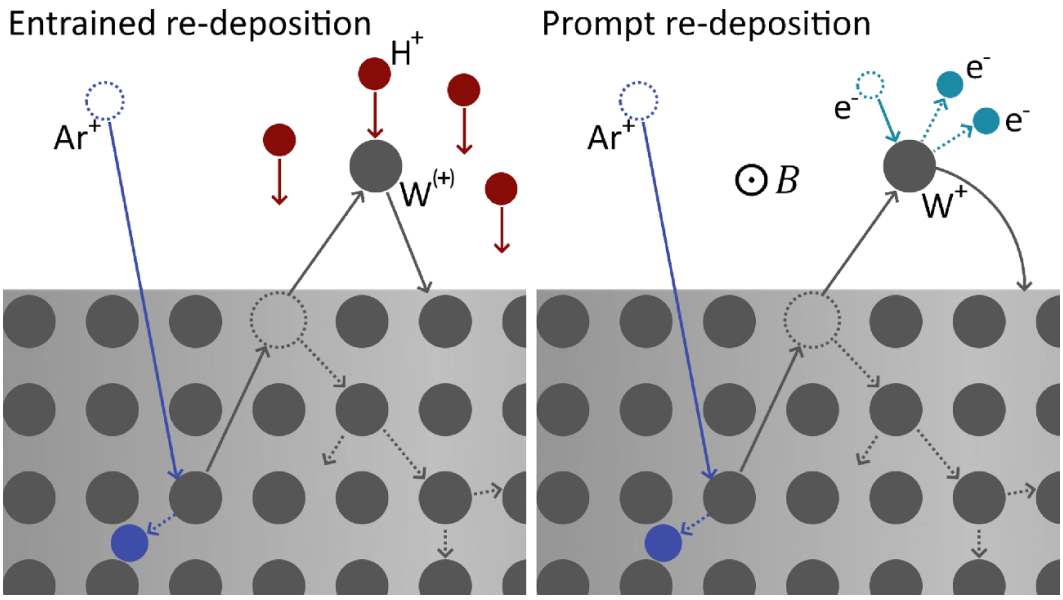

Figure 1. Schematic illustration of entrained and prompt re-deposition. In both figures, time flows from left to right. The direction of the magnetic field B is included.

assumption remains valid as long as the impurity concentration is small (<0.5% of the total ion density for heavy impurities such as W). The prompt re-deposition rate R_{prompt} is based on the likelihood that a sputtered particle becomes ionized at a certain angle and/or distance above the surface such that its gyro-orbit intersects with the target's surface, as described in [19]:

$$R_{\text{prompt}} = \frac{1}{1 + (\lambda_{\text{ion}}/\rho_{\text{i}})^2}. \tag{1}$$

Here, λ_{ion} is the ionization mean free path and ρ_{i} is the Larmor radius. Although this simplified expression does not account for multiple ionizations and the electric field within the magnetic pre-sheath and Debye sheath, the two effects mostly balance out for the plasma conditions studied here [20].

Whereas prompt re-deposition only occurs for ionized impurities, entrained re-deposition occurs for both neutral and ionized impurities. The entrainment of ionized impurities is caused by ion–ion Coulomb collisions, while for neutral impurities, the drag is driven by induced-dipole forces. Besides these forces, both electron and ion temperature-gradient forces are present, which typically point away from the target's surface, not toward it. Even though these forces can be substantial in the scrape-off layer of ITER [21], in Magnum-PSI, due to its relatively small temperature gradients [22], these temperature-gradient forces were negligible. The fraction of sputtered particles that re-deposit by entrainment is approximated as those that do not escape collisions:

$$R_{\text{ent}} = 1 - \mathrm{e}^{-p_{\text{ent}}}, \quad \text{where} \quad p_{\text{ent}} = \frac{L_{\text{plasma}}}{\lambda_{\text{mfp}}}. \tag{2}$$

Here, L_{plasma} is the characteristic length scale of the plasma, and λ_{mfp} is the mean free path between collisions. The full width at half maximum of the electron density profile w_{beam} can be estimated as L_{plasma}, as it corresponds to the distance a sputtered particle must travel from the center of the target to escape the plasma beam if it is emitted at an angle of 30° with respect to the normal of the target, under the condition that the plasma beam is inclined normal to the surface. To account for the likelihood that a sputtered particle becomes ionized or stays neutral, the reaction rate coefficient for charge exchange $\langle\sigma v\rangle_{\text{cx}}$, ionization $\langle\sigma v\rangle_{\text{io}}$ and recombination $\langle\sigma v\rangle_{\text{r}}$ are required. For ionization and recombination, the rate coefficients are acquired from the ADAS database [23] (ADF11/scd_W and ADF11/acd_W). For the plasma conditions considered here, recombination of W^+ was neglected, as $\langle\sigma v\rangle_{\text{r}} \ll \langle\sigma v\rangle_{\text{io}}$. Unfortunately, the charge-exchange rates and cross sections of W with H^+ and Ar^+ are not available, revealing a gap in the understanding of the ionization of W for low T_{e} plasmas. For $T_{\text{e}} \gtrsim 3$ eV, $\langle\sigma v\rangle_{\text{io}}$ is expected to be dominant over $\langle\sigma v\rangle_{\text{cx}}$. Analytical approximations of the charge-exchange cross sections between neutral H and fully stripped ions reveal cross sections in the same order of magnitude as the ionization cross section for low T_{e} plasmas [24], whereby the analytical expression is given by

$$\sigma_{\text{CX}} \approx 8\pi a_0^2 n_{\text{n}}^4 Z_{\text{i}} \left[1 + \sqrt{1/Z_{\text{i}}} + 1/4Z_{\text{i}}\right] \approx 1.6 \times 10^{-19}\text{m}^2. \tag{3}$$

Here, a_0 is the Bohr radius, $n_{\text{n}} = 1$ is the quantum level of the neutral, which is taken to be one to consider the ground state, and $Z_{\text{i}} = 1$ is the charge of the ion. Although such a crude extrapolation to the species of interest could be followed, the added uncertainty is expected to exceed the benefit of including the rates in the theoretical results presented here. However, due to the very low T_{e} plasmas investigated experimentally, the inclusion of charge exchange impacts the comparison between

theory and the experiment considerably. Therefore, values will be denoted with and without including the rough analytical extrapolations of the charge-exchange rates within the results section (section 5), but are not included within the theory section (section 2).

The fraction of particles that remain neutral or become ionized over time can be given by

$$P_{z,\mathrm{n}}(t) = \mathrm{e}^{-n_\mathrm{i}\left(\langle\sigma v\rangle_\mathrm{cx}+\langle\sigma v\rangle_\mathrm{io}\right)t}; \tag{4}$$

$$P_{z,\mathrm{i}}(t) = 1-\mathrm{e}^{-n_\mathrm{i}\left(\langle\sigma v\rangle_\mathrm{cx}+\langle\sigma v\rangle_\mathrm{io}\right)t}, \tag{5}$$

where $P_{z,\mathrm{n}}(t)$ and $P_{z,\mathrm{i}}(t)$ are the neutral-impurity and ion-impurity fractions over time, respectively, and n_i is the ion density. The typical dwell time t_D of a sputtered particle within the plasma, which is counted from the time that the sputtered particle leaves the surface, can be given by the following expression:

$$t_\mathrm{D} = \frac{\lambda_\mathrm{mfp}}{v_\mathrm{n}}. \tag{6}$$

Here, λ_mfp is the mean free path for collisions, and v_n is the velocity of the sputtered neutral perpendicular to the plasma beam. By factoring in the likelihood of a sputtered particle to stay neutral or become ionized within t_D, the mean free path λ_mfp is given by

$$\lambda_\mathrm{mfp} = P_{z,\mathrm{n}}(t_\mathrm{D})\,\lambda_\mathrm{ni} + P_{z,\mathrm{i}}(t_\mathrm{D})\,\lambda_\mathrm{ii} \tag{7}$$

where λ_ni is the mean free path for neutral particles and λ_ii for ionized particles. Using the corresponding collision rates, where $\langle\sigma v\rangle_\mathrm{ii}$ is the collision rate for ion–ion Coulomb collisions for the ionized particles and $\langle\sigma v\rangle_\mathrm{ni}$ is the collision rate coefficient for induced-dipole collisions for the neutral particles [9], the mean free path of the sputtered particles associated with entrainment is acquired:

$$\lambda_\mathrm{mfp} = P_{z,\mathrm{n}}(t_\mathrm{D})\,\frac{v_\mathrm{n}}{\langle\sigma v\rangle_\mathrm{ni}\,n_\mathrm{i}} + P_{z,\mathrm{i}}(t_\mathrm{D})\,\frac{v_\mathrm{n}}{\langle\sigma v\rangle_\mathrm{ii}\,n_\mathrm{i}}. \tag{8}$$

Particles that ionize within ρ_i from the target's surface, and participate in sufficient induced-dipole and/or ion–ion Coulomb collisions to re-deposit, are counted to re-deposit by both re-deposition mechanisms. Particles that ionize within ρ_i from the target's surface, but do not participate in sufficient collisions to re-deposit by those collisions, are only counted within the prompt re-deposition rate. Thus, although the total re-deposition rate is not given by the weighted sum of the entrained and prompt re-deposition rate, the re-deposition rates do provide a good comparison between the importance of both re-deposition mechanisms.

For the plasma-parameter regime of interest, figure 2 displays the theoretical re-deposition rates for prompt and entrained re-deposition. We consider neutral sputtered W to be introduced with an energy of $E_\mathrm{n} = 3$ eV, a common energy value for the bombardment of W by the impact of low-energy projectiles [25], and a velocity perpendicular to the plasma beam of $v_\mathrm{n} \approx \sqrt{E_\mathrm{n}/m_z}$. In addition, we consider $L_\mathrm{plasma} = 12$ mm, which corresponds to w_beam of the H plasma beams in Magnum-PSI and can be seen as a guestimated value related to the strikeline's width in tokamaks. The re-deposition rates suggest that for low-temperature plasmas ($T_\mathrm{e} \lesssim 3$ eV), entrained re-deposition takes precedence over prompt re-deposition. Although these conditions are expected during ITER's steady-state operation phase [5], the electron temperature can spike far above 100 eV during edge-localized modes (ELMs) [20]. ELMs lead to much shorter ionization lengths, and, consequently, elevated prompt re-deposition rates. Furthermore, the plasma becomes less collisional, reducing re-deposition by entrainment. Although the gross erosion rate significantly increases during ELMs, the contribution of the ELMs to the total net erosion depends on the achieved ELM regime. no-ELM and small-ELM regimes are being developed, which will be indispensable as a power exhaust solution for future fusion devices [26]. In this work, we focus on the steady-state plasma conditions, during which the erosion is driven by impurity bombardment.

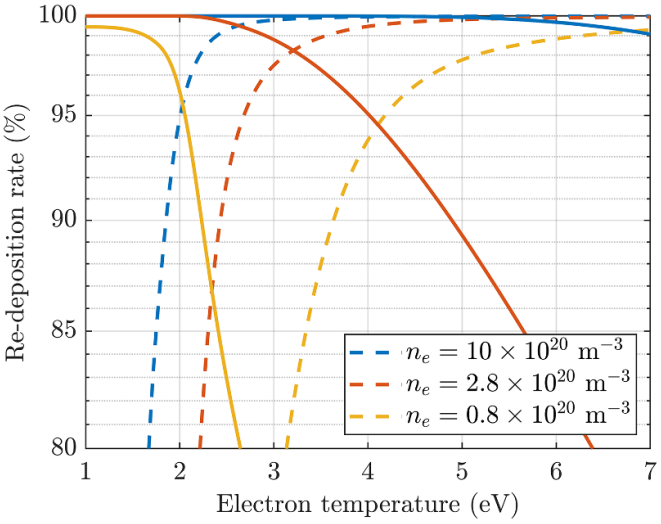

Figure 2. Theoretical predictions for the re-deposition rates for entrained re-deposition (solid) and prompt re-deposition (dashed) for different plasma conditions. Here, sputtered W impurities are considered to be introduced with an energy $E_\mathrm{n} = 3$ eV within a H plasma ($L_\mathrm{plasma} = 12$ mm and magnetic field parallel to the surface $B_\parallel = 1.2$ T).

3. Method

The experimental setup in Magnum-PSI is schematically depicted in figure 3. An in-depth description of Magnum-PSI can be found in [16, 17]. The Ar plasma beam was aligned with the center of the W target. The target was inclined at an angle of 45° relative to the plasma beam to be able to differentiate between prompt re-deposition and entrained re-deposition. Due to the angle between the magnetic field and surface normal, a magnetic pre-sheath is formed, also known as the Chodura sheath. The magnetic pre-sheath width scales with $\sin(\alpha)$, where α is the angle between the magnetic field

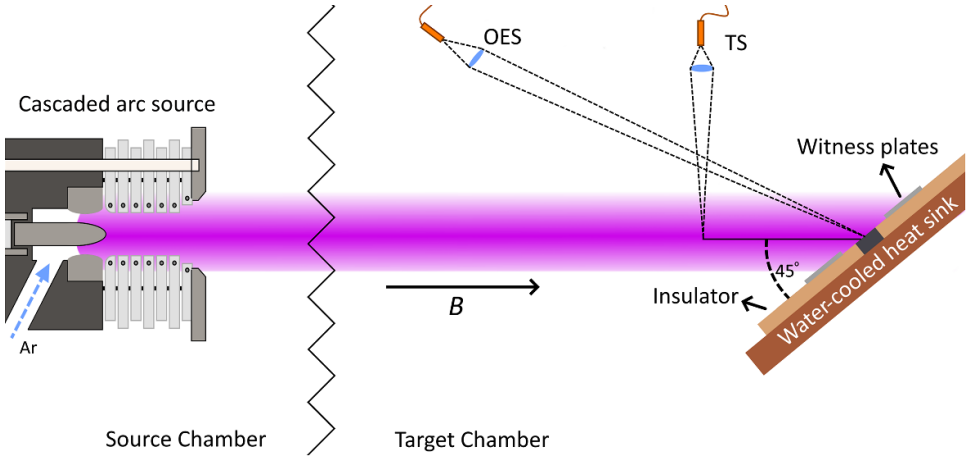

Figure 3. Schematic of the experimental setup in Magnum-PSI. Thomson scattering (TS) monitored the plasma parameters, while an optical emission spectrometer (OES) monitored emission from potential contamination.

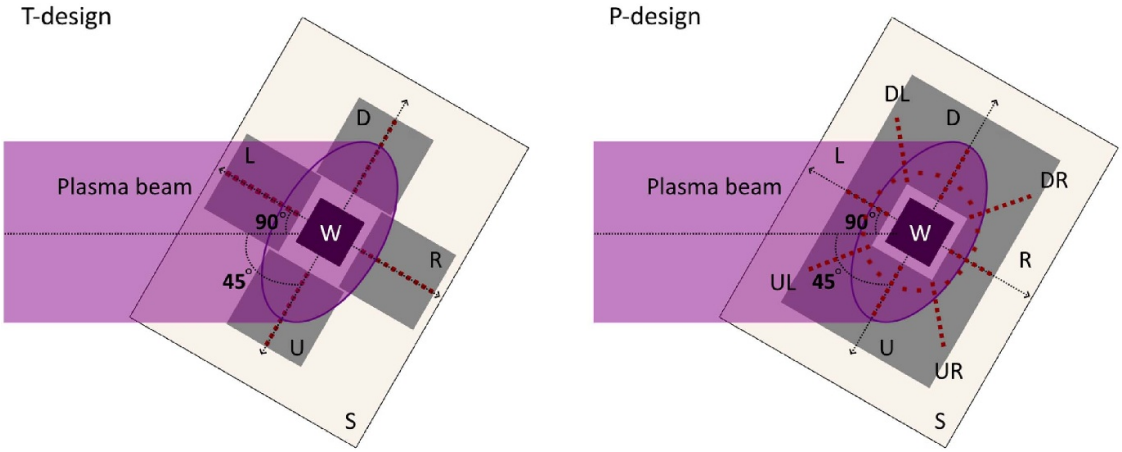

Figure 4. Schematic overview of the geometries with the four main directions: downstream (D), right (R), upstream (U), and left (L). For the T-design, RBS measurements were performed along the diameter of the witness plates (red dots). For the P-design, measurements were also made along the diagonals and circumference.

lines and surface normal. The magnetic pre-sheath impacts the re-deposition of tungsten by changing the ionization rate of sputtered impurities and by accelerating heavy impurities over a large distance [10]. Ar plasma exposures were chosen instead of impurity-seeded hydrogen isotope plasmas to acquire erosion rates significantly above the detection limit while keeping the required exposure time short enough. Within Magnum-PSI, radially outward electric fields can be present, which introduce $\vec{E} \times \vec{B}$ drifts in the anti-clockwise direction of figure 4. $\vec{B} \times \nabla \vec{B}$ drifts were not present due to the homogeneous magnetic field in Magnum-PSI.

In this section, first the target design and general diagnostics are discussed after which we focus on the ion beam analysis and mass balance to retrieve the re-deposition and erosion of W, respectively.

The 5 mm thick W target (10×10 mm) was surrounded by Mo witness plates, which were attached to a clamping plate made of insulating material (AlN-BN composite). Either four small witness plates (17×17 mm) were positioned around the W target (T-design, figure 4), or a single Mo plate (82×70 mm) encircled the W target (P-design, figure 4). The W target was clamped to the copper (Cu) heat sink and was biased to promote W erosion. The Mo witness plates were attached to the insulating material to ensure that they remained at floating potential, preventing their erosion during plasma exposure. To enhance heat conduction to the Cu heat sink, a thin eGraf® interlayer was positioned between the various components. Both the W targets and Mo witness plates were polished before exposure. A 5 μm trench with 1 μm markings was cut in the center of the W target with a focused ion beam (FIB, Carl Zeiss Crossbeam 540) before exposure (see figure 6, section 5.1).

Thomson scattering (TS) acquired the radial profiles of T_e and n_e ~9 cm in front of the target's surface, giving $w_{beam} \approx$ 25 mm for the Ar plasma exposures investigated. Therefore, the plasma beam was much broader than the W targets, making misalignments less prone to occur. Specifications of the TS system can be found in [27]. A pyrometer (FAR-Associates FMPI Spectropyrometer) monitored the surface temperature to ensure that neither the W target nor the Mo witness plates

(re-)evaporated significant amounts of W. An optical emission spectrometer (OES, Avantes AvaSpec-2048-USB2) was used to monitor emission from potential contamination within the wavelength range of 378–558 nm. Neither significant contamination nor erosion of the witness plates and insulating material was found. In addition to the operando diagnostics, several pre- and post-exposure analysis techniques were used to monitor the erosion and re-deposition of W: (1) the deposition profile was studied using Rutherford Backscattering Spectroscopy (RBS), (2) the mass loss of the W target was acquired using a microbalance, (3) changes in surface morphology and micro-trench depth were observed through scanning electron microscopy (SEM, Carl Zeiss CrossBeam 540) with the secondary electron detector, (4) the elemental composition of the surface was determined using energy dispersive x-ray spectroscopy (EDX, Oxford Instruments X-Max 80), and finally (5) changes in surface roughness were measured with a profilometer with a KF3 sensor from OPM Messtechnik GmbH. This laser profilometer measured the arithmetical mean surface roughness S_a, which was defined according to the ISO 4287.

3.1. Ion beam analysis

Post-exposure, the witness plates were examined ex-situ with RBS. A beam of 2.4 MeV He^3 or He^4 ions with a spot size of 1×1 mm was aimed perpendicular to the surface. The measurement positions on the witness plates are depicted in figure 4. The RBS detector was positioned in IBM geometry. For the small witness plates (T-design), the exit angle was 10.3° and the particles × steradian was set at ≈3700 pr sr. For the single large witness plate (P-design), the exit angle was 21.5° and the particles × steradian was set at ≈2950 pr sr.

To retrieve the deposited W, the RBS spectra were analyzed with SIMNRA [28]. The uncertainty in the Poisson noise, measurement setup (solid angle, calibration, and scattering angle), and the fitting procedure were all considered in the 95% confidence intervals of the total amount of deposited W.

3.2. Mass balance

The W targets were weighed before and after plasma exposure with a micro-balance (Metler Toledo NewClassic MF MS105DU), which has a mass resolution of 0.01 mg. 95% uncertainty intervals in the weighing procedure were acquired by weighing the targets at least five times. The lost mass gave the net-eroded mass Δm_n. The gross-eroded mass Δm_g was calculated based on the sputtering yield Y_{Ar} by the incident Ar-ion flux Γ_{Ar}. The sputtering yield Y_{Ar} was based on the sputtering yield curves for normal incidence documented in [31], considering that the magnetic pre-sheath turns the ion flow from parallel to the magnetic field to normal to the surface and that the magnetic pre-sheath is considerably thicker than the surface roughness. In addition, for a rough surface with a mean inclination angle δ_n of the surface of ∼45° or lower, the sputtering yield is fairly insensitive to the angle of incidence [32]. The Ar-ion impact energy, which is required to retrieve the sputtering yield Y_{Ar}, was based on [9]

$$E_i = \frac{5}{2} k_B T_e - eV_{bias}, \tag{9}$$

where V_{bias} is the applied bias voltage to the W target. The incident Ar-ion flux Γ_{Ar} was determined from the Bohm criterion [29]:

$$\Gamma_{Ar} = \sin(\theta) \frac{1 + M_u}{2} \sqrt{\frac{k_B (T_e + \gamma T_i)}{m_i}}, \tag{10}$$

where $\theta = 45°$ is the angle between the magnetic field lines and the surface normal, M_u is the Mach number at the TS location, γ is the adiabatic factor and m_i is the ion mass. We assume that $M_u = 0$, $T_e = T_i$, and that there is no significant energy loss between the TS measurement location and the target surface. Assigning a single value to γ is difficult, as it varies within the sheath region [30]. However, for consistency, $\gamma = 1$ is assumed. The gross eroded mass is given by

$$\Delta m_g = Y_{Ar}(E_i) \Gamma_{Ar} m_W A_W t_D, \tag{11}$$

where m_W is the atomic mass of tungsten, A_W is the surface area of the tungsten target and t_D is the exposure time. Only sputtering by the incident Ar particles was considered, as the Ar plasma beam contained negligible amounts of other impurities according to the optical emission spectrometer (OES). W self-sputtering was insignificant for the conditions under investigation as $Y_{Ar} < 0.05$ and as the self-sputtering yield of W was an order of magnitude smaller compared to Y_{Ar} for the ion impact energies under investigation. Based on Δm_n and Δm_g, the local re-deposition rate R is given by

$$R = 1 - \frac{\Delta m_n}{\Delta m_g}, \tag{12}$$

which is considered to be local as only re-deposition on the W target itself is included.

4. Procedure

A summary of the plasma exposures is presented in table 1. The spatially averaged values of T_e and n_e across a 10 mm space centered around the W target are tabulated. The variation of T_e and n_e within this region was small (see supplementary data) as the plasma beam was considerably broader than the 10×10 mm tungsten target ($w_{beam} \approx 25$ mm). In addition, the magnetic field of 0.8 T for exposures T1–T4 was increased to 1.2 T for exposure P to achieve a higher incident Ar-ion flux. The exposure time was selected such that a similar amount of gross erosion was expected between the exposures but exposure T1, for which a prolonged exposure was done.

Table 1. Overview of the exposures investigated: T_e—electron temperature, n_e—electron density, Γ_{Ar}—incident Ar-ion flux, E_i—Ar-ion impact energy, t_D—exposure time. A constant uncertainty of ± 3 eV was assigned to E_i to account for uncertainties in the sputtering yield curves and formulation of E_i. The uncertainty within t_D is determined from the beam dump system. For the other quantities, the standard variations are given based on the spatial averaging and the variation between TS measurements during one steady-state plasma exposure.

Species (ID)	T_e (eV)	n_e (10^{20} m^{-3})	Γ_{Ar} (10^{23} m^{-3})	E_i (eV)	t_D (s)
Ar (T1)	1.13 ± 0.04	3.8 ± 0.2	3.1 ± 0.2	43 ± 3	8134 ± 1
Ar (T2)	1.14 ± 0.04	4.4 ± 0.2	3.7 ± 0.2	44 ± 3	3897 ± 1
Ar (T3)	1.11 ± 0.05	4.4 ± 0.2	3.6 ± 0.2	63 ± 3	523 ± 1
Ar (T4)	1.14 ± 0.04	4.4 ± 0.3	3.7 ± 0.2	94 ± 3	72 ± 1
Ar (P)	1.27 ± 0.04	7.5 ± 0.7	6.6 ± 0.6	64 ± 3	320 ± 1

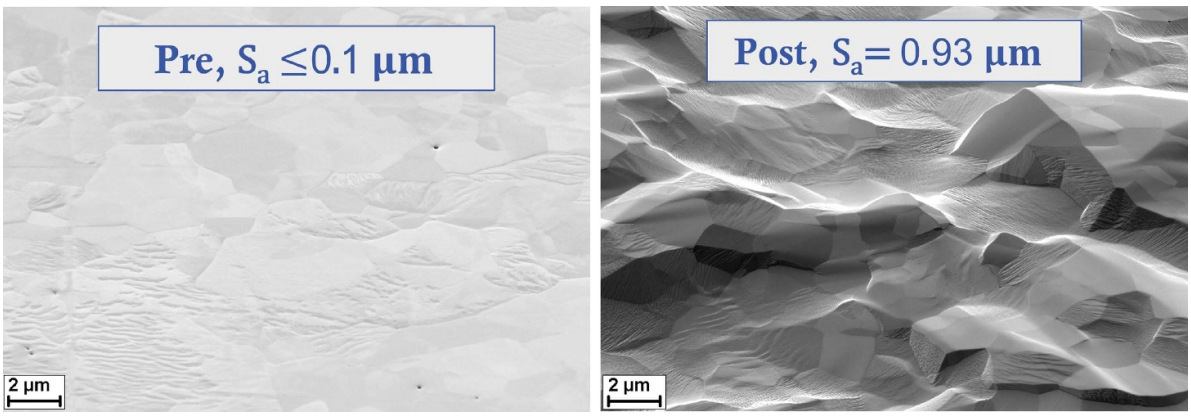

Figure 5. SEM images showing plasma-induced roughening of the W target's surface (T4, pre- and post-exposure). The surface roughness was quantified with a profilometer, which determined the arithmetical mean height S_a of the central part (1×1 mm) of the W target's surface. Images show the same location.

Table 2. Overview of the local re-deposition rates for each exposure: E_i—Ar-ion impact energy, S_a—arithmetical mean surface roughness. Δm_n—net eroded mass, Δm_g—gross eroded mass, R—local re-deposition rate. The uncertainty interval of R is given by the super- and sub-scripted values. The local re-deposition rate decreases for higher ion-impact energies (T1–T4), but increases for higher electron densities (T3, P).

Species (ID)	E_i (eV)	S_a (μm)	Δm_n (mg cm^{-2})	Δm_g (mg cm^{-2})	R (%)
Ar (T1)	43 ± 3	0.57 ± 0.01	4.81 ± 0.03	69 ± 35	93^{+2}_{-8}
Ar (T2)	44 ± 3	0.52 ± 0.01	4.24 ± 0.01	47 ± 23	91^{+3}_{-8}
Ar (T3)	63 ± 3	0.54 ± 0.01	6.04 ± 0.02	49 ± 12	88^{+2}_{-4}
Ar (T4)	94 ± 3	0.87 ± 0.06	11.56 ± 0.03	36 ± 5	68^{+4}_{-5}
Ar (P)	64 ± 3	—	4.07 ± 0.02	58 ± 14	93^{+1}_{-2}

5. Results

5.1. Surface analysis

The plasma exposures increased the surface roughness of the W targets from $S_a \leqslant 0.1$ μm to $S_a = 0.5$–0.9 μm, as visualized in figure 5. Sputtering by the Ar plasma beam resulted in a mountain-like surface for which the grain boundaries were still clearly present. Targets T1–T3 have a similar topography but with a lower surface roughness of $S_a = 0.52$–0.57 μm compared to target T4. An overview of the surface roughnesses is tabulated in table 2.

Based on the profilometry measurements, the erosion occurred homogeneously along the W target's surface, corresponding well to the relatively flat n_e and T_e profiles around the target's position and the broad plasma beam.

For exposure T2 and T4, the µm-trench could not be identified after exposure, meaning that they are completely eroded and/or filled with re-deposited material. The µm-trenches of T1 and T3 are depicted in figure 6, before and after exposure. The µm-trenches appear to be both eroded and simultaneously filled with re-deposited material. Since the µm-spaced markings were no longer visible, precise measurements of the eroded thickness were not obtained. Nevertheless, the results reveal that erosion and re-deposition occurred on the µm-scale.

5.2. Net and gross erosion

The net and gross erosion of the W targets are tabulated in table 2. For target T4 the net eroded mass is significantly larger compared to the other targets, resulting in a higher surface

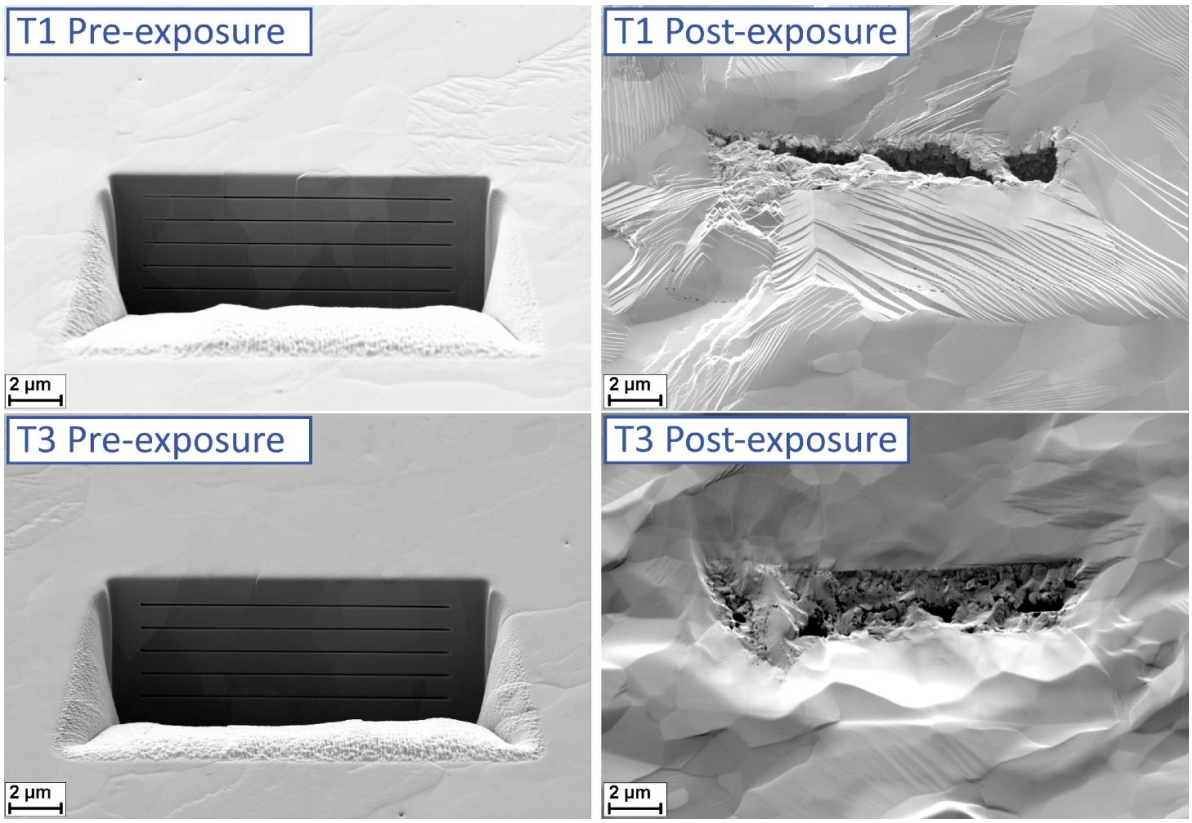

Figure 6. SEM images of the W targets showing the erosion of their µm-trenches and the re-deposition of tungsten into the µm-trenches. Furthermore, roughening is evident, though less pronounced than for target T4 (figure 5). Pre- and post-exposure images show the same location.

Table 3. An overview of the re-deposition lengths that are coupled to the erosion mechanisms: E_W—average kinetic energy of the sputtered W particles, $\lambda_{ent,ii}$—ion–ion Coulomb collision entrainment length, $\lambda_{ent,ni}$—neutral-ion induced-dipole entrainment length, λ_{ion}—ionization mean free path (with/without the inclusion of charge exchange), ρ_i—Larmor radius. The drag forces by Coulomb collisions and induced dipoles are considered separately to distinguish between ionized and neutral impurities.

Species (ID)	E_W (eV)	$\lambda_{ent,ii}$ (mm)	$\lambda_{ent,ni}$ (mm)	λ_{ion} (mm)	ρ_i (mm)
Ar (T1)	2.6 ± 0.4	0.08 ± 0.02	3.1 ± 1.2	$13.9 \pm 0.8/85 \pm 8$	4.0 ± 0.3
Ar (T2)	2.8 ± 0.4	0.08 ± 0.02	2.8 ± 1.0	$12.1 \pm 0.6/76 \pm 7$	4.1 ± 0.3
Ar (T3)	4.7 ± 0.4	0.13 ± 0.02	4.8 ± 1.2	$12.5 \pm 0.6/98 \pm 8$	5.3 ± 0.2
Ar (T4)	7.4 ± 0.3	0.21 ± 0.03	7.6 ± 1.9	$12.9 \pm 0.9/123 \pm 12$	6.7 ± 0.1
Ar (P)	4.8 ± 0.4	0.09 ± 0.01	2.7 ± 0.6	$7.3 \pm 0.7/56 \pm 9$	3.6 ± 0.1

roughness. The net eroded thickness of target T4 exceeds the complete depth of the μm-trench, corresponding well to the loss of its µm-trench. The local re-deposition rate decreased strongly from ∼93% to ∼68% as the Ar-ion impact energy increased from 43 eV to 94 eV. In addition, exposure T3 and exposure P reveal that the local re-deposition rate increased with the electron density.

To ascertain the significance of each re-deposition mechanism, an overview of the typical length scales associated with entrained and prompt re-deposition is presented in table 3. The ionization length and its derived quantities are shown with and without the inclusion of the extrapolated charge exchange rates between H and W^+ from equation (3), here applied to W and Ar^+. Without including charge-exchange, the ionization length becomes so long that the re-deposition of ionized sputtered tungsten would be negligible, which is unlikely given the left-right asymmetry in the re-deposition profiles (figure 9), as explained in section 5.3. Therefore, we focus on the values tabulated for which the extrapolated charge-exchange rates are included. As surface roughening by plasma exposure does not indicate any orientation preference for the sputtering direction, and the magnetic pre-sheath ensured that the ions impacted the surface orthogonal on a macroscopic scale, the sputtered atoms were assumed to be distributed isotropically. Although a Thompson energy distribution could be used to retrieve the energy of the sputtered W, the tail of the Thompson energy distribution does not correspond well with experimental results for the bombardment of W by low Ar-ion impact energies [33]. Therefore, we opted to use the mean energy of sputtered W E_W documented in [25]. The energy of the sputtered W atoms increases for increasing Ar-ion impact energies as the W particles are ejected from

Table 4. Comparison between the experimental and theoretical re-deposition rates: R_{prompt}—theoretical prompt re-deposition rate (with/without the inclusion of charge exchange), R_{ent}—theoretical entrained local re-deposition rate (with/without charge-exchange included), R—experimental local re-deposition rate.

Species (ID)	R_{prompt} (%)	R_{ent} (%)	R (%)
Ar (T1)	4/0.1	89/86	93^{+2}_{-8}
Ar (T2)	4/0.1	92/89	91^{+3}_{-8}
Ar (T3)	5/0.1	86/81	88^{+2}_{-4}
Ar (T4)	7/0.1	80/74	68^{+4}_{-5}
Ar (P)	4/0.4	97/94	93^{+1}_{-2}

the surface with more energy. The particles were deemed entrained if their velocity parallel to the magnetic field was reduced to zero. We consider that the W particles are ejected from the surface with a typical velocity of $v_{\perp} = v_{\text{W}}/\sqrt{2}$ parallel to the magnetic field. The descriptions of the ion–ion Coulomb collision ($\lambda_{\text{ent,ii}}$) and the ion-neutral collision ($\lambda_{\text{ent,ni}}$) entrainment lengths are addressed in the companion paper [9].

As neutral impurities are not dragged by the strong ion–ion Coulomb collisions, but by the weaker induced-dipole force, the drag on neutrals is smaller than for the ions. Nevertheless, even before ionization, a considerable amount of entrained re-deposition occurred, as $\lambda_{\text{ent,ni}} < \lambda_{\text{ion}}$. After ionization, the sputtered W atoms are quickly dragged back to the surface and are generally unable to complete their gyro orbits as $\lambda_{\text{ent,ii}} \ll \rho_{\text{i}}$. Consequently, entrained re-deposition is anticipated to be dominant over prompt re-deposition for the exposures investigated. The theoretical prompt and entrained re-deposition rates are summarized and compared with the experimental local re-deposition rates in table 4. To acquire the theoretical entrained re-deposition rate R_{ent}, we take $L_{\text{plasma}} = 5$ mm to only consider entrained re-deposition onto the target itself for the given geometry. For all exposures, $R_{\text{ent}} >> R_{\text{prompt}}$. In addition, R_{ent} corresponds well to the experimentally acquired local re-deposition rate R.

A clear decreasing trend in R was found by increasing E_{i} between exposures T1–T4, which can be attributed to an increase in E_{W}. When E_{W} increases, both entrainment lengths ($\lambda_{\text{ent,ii}}$ and $\lambda_{\text{ent,ni}}$) become longer, indicating that entrained re-deposition is impeded as the sputtered particles have a larger probability to escape the plasma beam before becoming entrained with the plasma flow. Furthermore, the Larmor radius ρ_{i} increases for increasing E_{W}, resulting in a broader re-deposition profile for prompt re-deposition, thus leading to a lower local re-deposition rate. Finally, by comparing exposure T3 to P, a relatively high R was found if n_{e} was solely increased. As n_{e} increases, the collisionality of the plasma is enhanced, leading to more re-deposition by entrainment. In addition, the probability for an ionization event to occur is enhanced, leading to both more prompt re-deposition and entrained re-deposition by the same reasoning as outlined before.

5.3. Re-deposition profiles

The re-deposition of W on the Mo witness plates was investigated with ion beam analysis. The data was analyzed using SIMNRA 7.03 [28], in which a simulated depth profile was matched to the experimental data (figure 7). The spectra of a pure Cu, Mo and W sample were analyzed to calibrate the RBS measurements. The high-energy peak in the RBS spectra shows the amount of deposited W, whereas the lower-energy signal with a sharp edge originates from the Mo witness plate. Typically, four layers were considered: a heavily oxidized thin W surface layer (∼50%–70% O), a layer containing mainly W but mixed with O and small amounts of Mo (0%–10% Mo), a transition layer primarily composed of Mo with some W (0%–30% W), and the pure Mo substrate. As the amount of deposited W scales with the counts of the high-energy peak, the assumptions in the SIMNRA depth profile do not significantly affect the results, but help to guide the analysis when the high-energy peak and lower-energy signal start to overlap.

Even though some redundancy was noted between the roughness and porosity of the layers, the influence of these parameters on the retrieved amount of deposited W was minimal. The diminishing width and ultimately height of the high-energy peak shows a strong reduction in W deposition when moving further away from the W target's surface. For minimal amounts of W deposition (≪150 nm), the high-energy peak was manifested as a distinct and separate peak. However, for thicker W layers (⩾150 nm), the W and Mo contributions to the RBS spectrum start to overlap mainly due to surface roughness, resulting in greater uncertainties in the amount of deposited W. The high-energy peak exhibited a broader low-energy tail than anticipated from roughness and porosity alone, indicating the presence of Mo within the W top layer.

In addition to the RBS measurements, several μm-trenches were cut post-exposure in the Mo witness plate of the P-design. SEM and EDX images of the μm-trench made 2 mm upstream of the W target are displayed in figure 8, together with the corresponding RBS spectrum. The SEM and EDX images show the deposition of a 200–270 nm thick W layer on the Mo witness plate. The EDX images indicate the mixing of the Mo with the deposited W, in accordance with the RBS measurements. In addition, the deposited amount of W measured by RBS aligns with the EDX images, given that the W layer consists of ∼40% W according to the RBS spectrum. The surface of the deposited W layer appears to be porous and rough, supporting the incorporation of porosity and roughness in the SIMNRA simulations. The deposited W migrates along the grain boundaries of the Mo

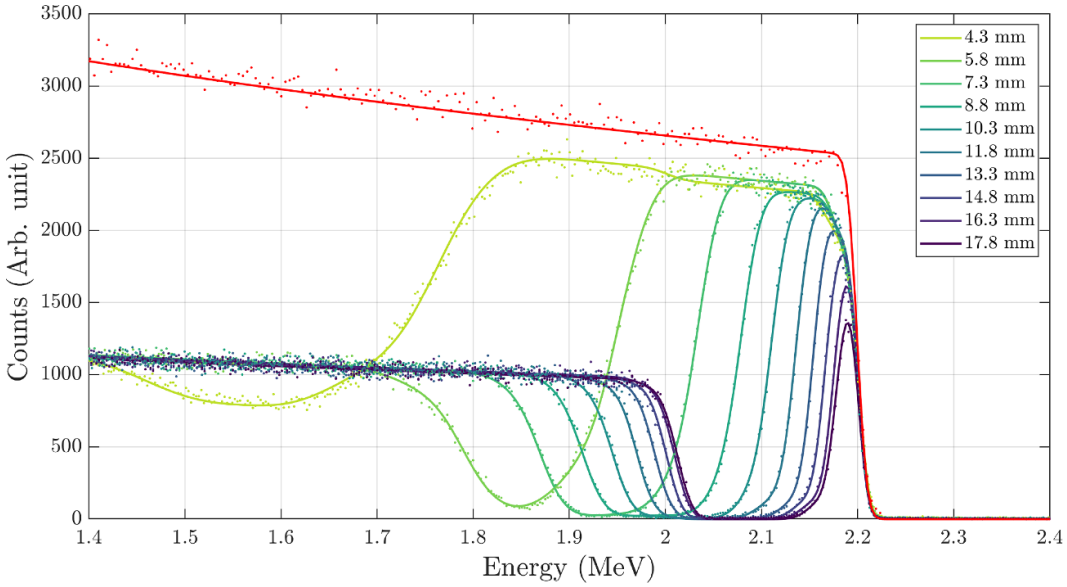

Figure 7. Measured RBS spectra (dots) and simulated RBS spectra (lines) along the diameter of the witness plate positioned to the right of the W target for exposure T4. The legend shows the distance to the W target. In red, the RBS spectrum of a pure W reference sample is shown. The decrease in width and height of the high-energy peak shows a strong reduction in the W content as the distance to the W target increases.

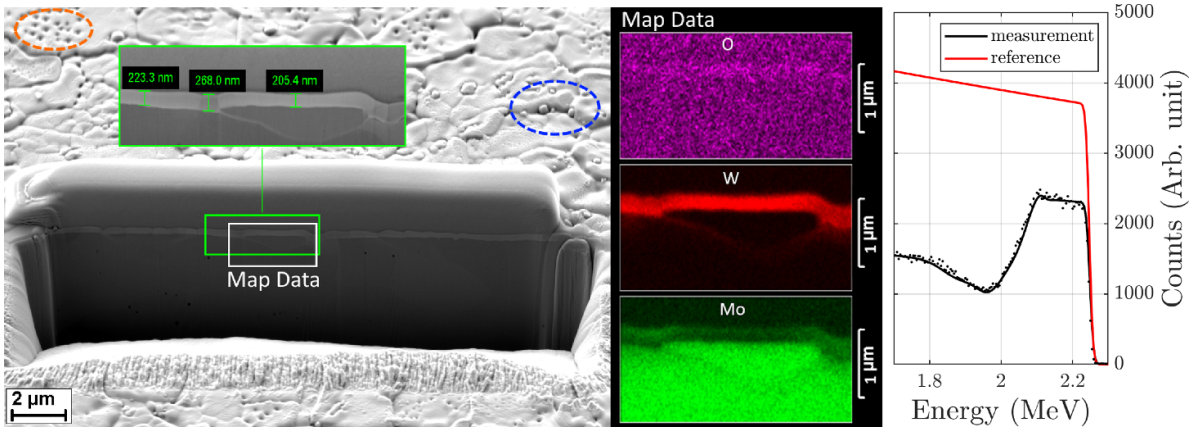

Figure 8. (left) SEM and EDX images of a µm-trench made in the Mo witness plate 2 mm upstream from the W target's surface after exposure P; right) RBS spectrum made from the same location (black) with a reference spectrum for a pure W sample (red). The surface area of the cross section was coated with a thin platinum layer before FIB milling. Some pits (orange encircled) and an emphasized grain boundary (blue encircled) are highlighted.

witness plates, indicating fast diffusion of W along the grain boundaries, which may also be important for tritium diffusion. Finally, small pits were found to be present of around 0.1–1 µm.

The re-deposition profiles were obtained by combining the RBS results along the upstream (U), downstream (D), right (R), and left (L) diameters of the witness plates, and are shown for each exposure in figure 9. For all exposures, and along all directions, the deposited amount of W follows an exponential decrease when moving away from the W target's surface. For exposure P, the re-deposition profile is much narrower and steeper compared to exposure T1–T4, aligning well with the shorter length scales associated with both entrained and prompt re-deposition for the relatively high n_e of exposure P. The re-deposition profiles for exposures T1–T4, which have similar n_e and T_e, show very similar re-deposition profiles (figure 11).

Although misalignments of the plasma beam with respect to the target could result in asymmetries within the re-deposition profile, asymmetric erosion of the W targets was not observed from profilometry. In addition, no large variations in T_e and n_e were found across a 10 mm diameter around the center of the plasma beam. Therefore, alternative explanations for the observed asymmetries are outlined below.

For all exposures, a prominent up-downstream asymmetry was found in the re-deposition profile, with more W deposition in the downstream than the upstream direction. The up-downstream asymmetry is attributed to entrained re-deposition. Considering the direction of the plasma flow with respect to the normal of the surface, entrainment

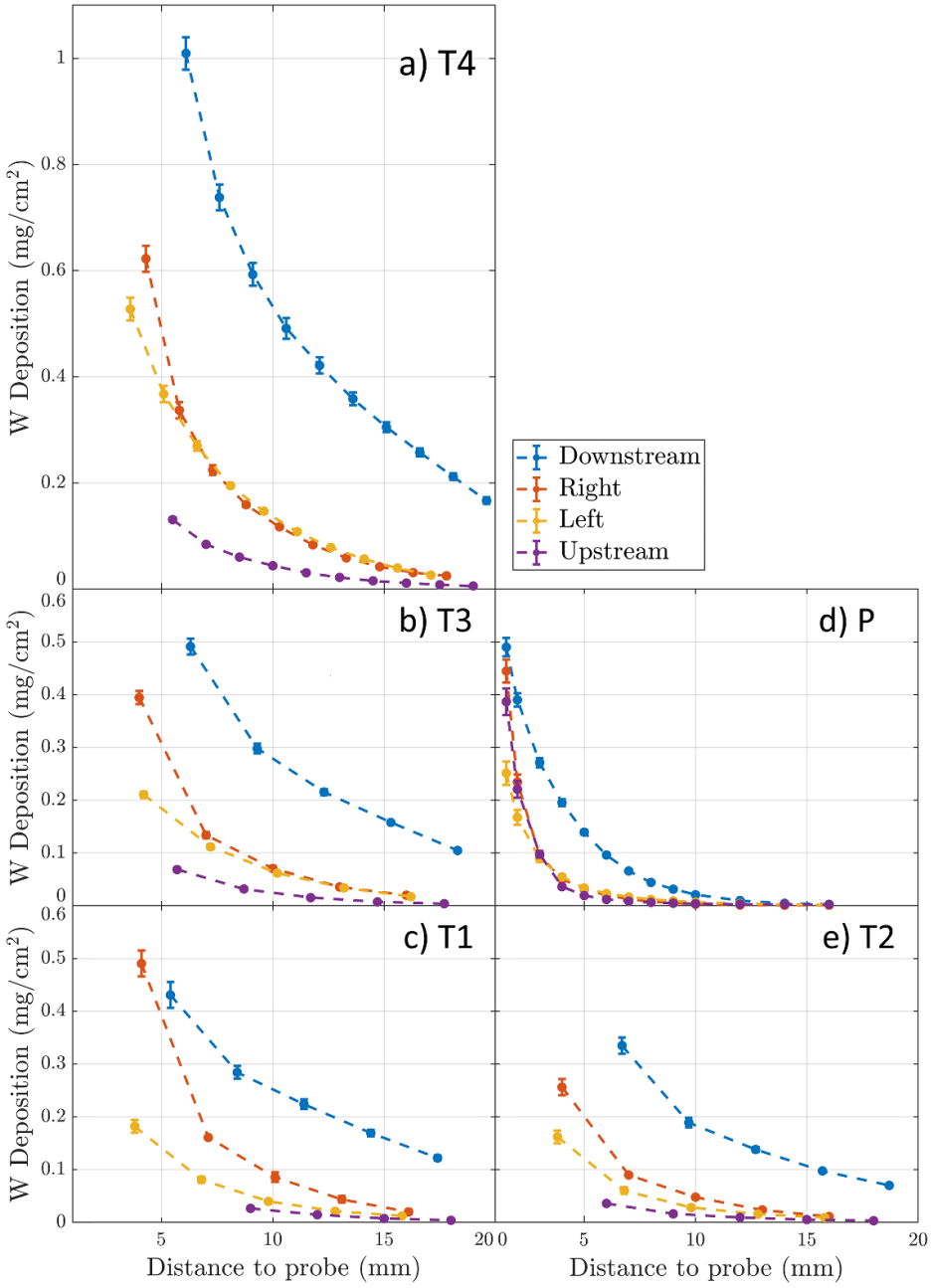

Figure 9. Amount of deposited W on the Mo witness plates as traced along their diameters (as shown in figure 4) for each exposure: (*a*) exposure T4 with high E_i and low n_e; (*b*) exposure T3 with mid E_i and low n_e; (*c*) exposure T1 with low E_i and low n_e; (*d*) exposure P with mid E_i and high n_e; (*e*) exposure T2 with low E_i and low n_e. The legend corresponds to the discharges in table 1. A distinct up-downstream asymmetry is present in the re-deposition profile, which is attributed to entrained re-deposition. The left-right asymmetry is subtler and grows in prominence for lower ion-impact energies.

drags the impurities downstream. The strong up-downstream asymmetry reveals that entrained re-deposition was dominant over prompt re-deposition, which is consistent with the theoretical expectations for the plasma conditions considered here (table 4).

Furthermore, near the W target, a less pronounced left-right asymmetry was found in the re-deposition profile. The left-right asymmetry is present at a smaller distance away from the surface with increasing E_i (figure 9). Considering the geometry and the electric and magnetic fields present, this left-right asymmetry is most probably related to the migration of ionized sputtered tungsten particles. In Magnum-PSI, a radially outward electric field is commonly present. However, the $\vec{E} \times \vec{B}$ drift introduced by this radial electric field would result in an asymmetric profile with more re-deposition to the left, which is not observed. The $\vec{E} \times \vec{B}$ drift introduced by the electric field within the magnetic pre-sheath does result in a drift to the right, which corresponds to the observed left-right asymmetry. In addition, the left-right asymmetry might be associated with the gyro-motion of the ionized sputtered

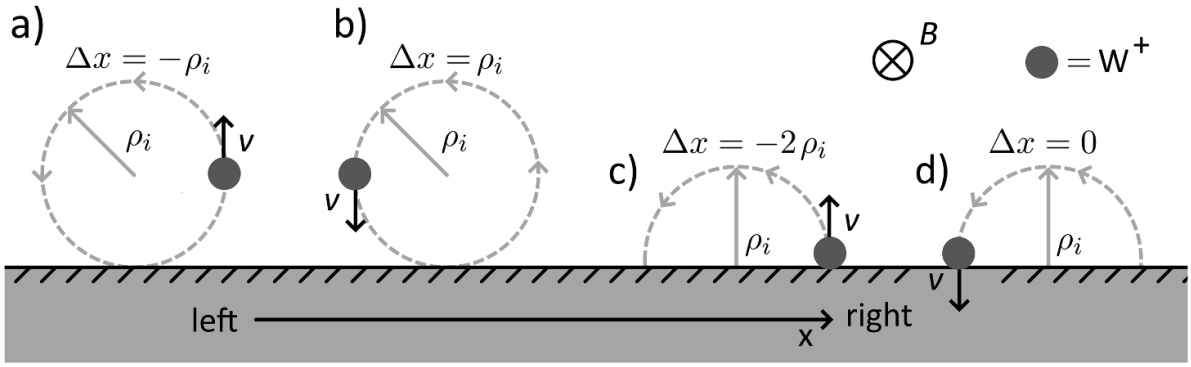

Figure 10. The gyration of ionized W in the presence of a static magnetic field B. The left-right convention is the same as in figure 4. Only particles that are ionized at a Larmor radius ρ_i from the surface (a), (b) and at no distance from the surface (c), (d) are considered. Without collisions, particles that ionize while moving away from the surface deposit to the left (a: $\Delta x = -\rho_i$, c: $\Delta x = -2\rho_i$), while particles that ionize while moving towards the surface deposit to the right (b: $\Delta x = \rho_i$, d: $\Delta x = 0$).

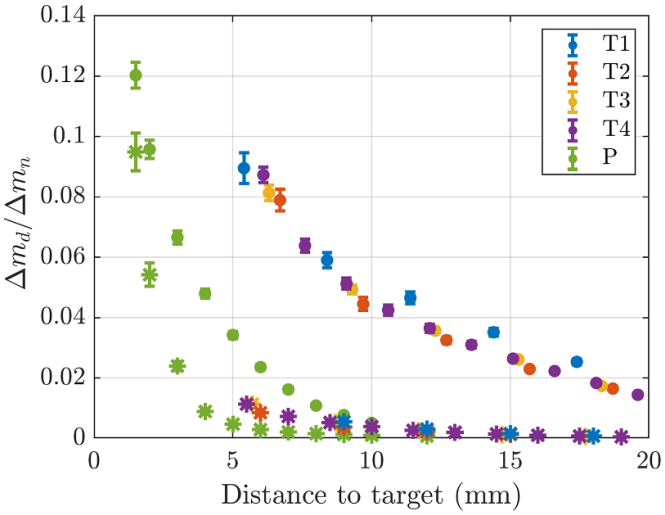

Figure 11. The ratio of the deposited W to the net eroded W ($\Delta m_d/\Delta m_n$) for the downstream (circles) and upstream (stars) direction. This ratio provides insight into the amount of deposited W for each net eroded W, offering a measure to compare the re-deposition profiles.

particles, as an incomplete gyro-motion results in a drift perpendicular to both the magnetic field lines and normal of the surface, as illustrated in figure 10. Given the highly collisional nature of the plasma ($\lambda_{ent,ii} \gg \rho_i$), the gyro-orbits are typically far from completed. In addition, the drag on neutral sputtered tungsten was significant, and therefore ionization mostly occurs after the sputtered particle already has a velocity towards the surface. Therefore, on average, the in-complete gyro-motions of ionized sputtered tungsten particles can result in a drift towards the right.

The degree to which the up-downstream asymmetry is present remains the same for exposure T1–T4. Thus, E_i did not influence the up-downstream asymmetry (figure 11) and thereby did not influence the entrained re-deposition profile. Although E_i did strongly influence the local re-deposition rates as acquired by the mass balance and the amount of deposited W from RBS, E_i only slightly affects the re-deposition profile concerning its left-right asymmetry. Finally, a higher electron density enhances the collisionality of the plasma, thereby increasing the probability of both prompt and entrained re-deposition closer to the target. This results in the narrower re-deposition profile observed for exposure P compared to exposures T1–T4, and the higher re-deposition rate of exposure P, which is in line with the previous results.

6. Implications for ITER

Maintaining low net erosion rates will be crucial for ITER to ensure a long lifetime for the plasma-facing components and achieve good plasma performance. Research conducted at JET revealed prompt re-deposition rates exceeding 94% for full W divertors [11], thereby greatly reducing the net erosion rate. During ITER's operation phase, prompt re-deposition will remain crucial, especially during ELMs, as T_e is elevated and λ_{ion} is relatively short during ELMs. However, during steady-state operation, characterized by high-density ($n_e > 2 \times 10^{20}$ m^{-3}) and low-temperature ($T_e < 5$ eV) divertor plasma conditions, entrained re-deposition is anticipated to become the dominant re-deposition mechanism due to the highly collisional nature of the near-surface plasma region. Furthermore, the high density of ITER's divertor plasma [5] will promote a narrow re-deposition profile. Without drifts, entrained re-deposition is local for the tokamak geometry, as entrained re-deposition promotes re-deposition in the downstream direction, which remains within the plasma exposed region given the toroidally symmetric strike line. However, $\vec{E} \times \vec{B}$ drifts have an important impact on the W re-deposition due to the grazing incidence of the magnetic field with respect to the plasma-facing components. These drifts adjust the migration of sputtered W, resulting in shadowed re-deposition [34]. In addition to the $\vec{E} \times \vec{B}$ drifts, ion $\vec{B} \times \nabla \vec{B}$ drifts will be present. These drifts change the plasma flows favorable or unfavorable depending on the toroidal magnetic field direction [35]. A change in the plasma flow affects the force balance between the frictional forces and the temperature gradient forces, of which the latter tends to drive impurities from the divertor region to the upstream region in tokamaks.

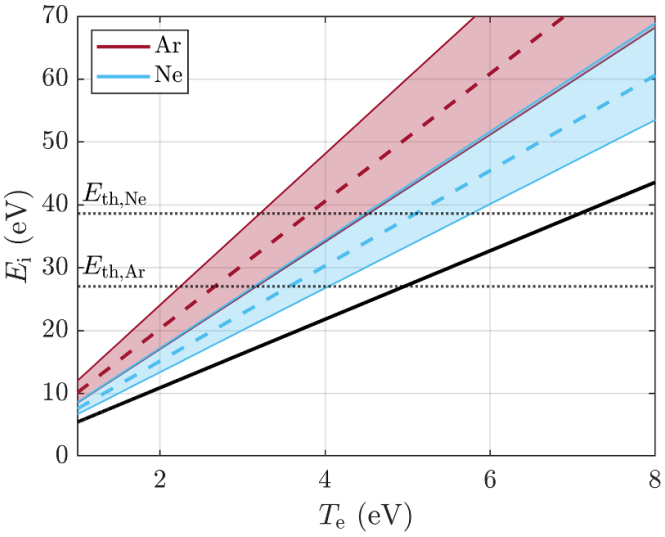

Figure 12. The impurity-impact energy for Ar (red) and Ne (blue) impurities. The black line indicates the situation without impurity entrainment, while the shaded areas indicate the situation for which entrainment is considered ($M_{se} = 0.55$–0.75). The colored dotted lines indicate the situation for which $M_{se} = 0.65$. The horizontal black dotted lines show the threshold energies for sputtering as retrieved from [31].

The experiments in Magnum-PSI were conducted using pure Ar plasmas with biased W targets to promote erosion, while ITER will utilize Ne seeded D:T plasmas [5]. Furthermore, the angle with the magnetic field was 45° instead of the grazing angle for ITER. Nevertheless, given the good agreement between theory and experiments, the theoretical framework is applied to extrapolate the results, while keeping in mind that charge-exchange reactions, drifts and temperature gradient forces are not included within this model. The theoretical framework indicates that under ITER-like H divertor plasma conditions, with $n_e = 10^{21}$ m^{-3}, re-deposition rates exceeding 99% (figure 2) are expected, for which the re-deposition is predominantly promoted by entrainment for low-T_e ($\lesssim$4 eV) and by prompt re-deposition for high-T_e ($\gtrsim$5 eV) plasma conditions. However, a more precise assessment of the re-deposition rate under ITER-like divertor plasma conditions necessitates experiments using impurity-seeded hydrogen isotope plasmas. In addition, models that include the drifts and temperature gradient forces will be required to accurately extrapolate the experimental results from Magnum-PSI to ITER's operation phase. Finally, for a complete understanding of the migration of sputtered W and its simulation, the exact charge-exchange rates between sputtered W and H^+, D^+ and T^+ will be required.

Entrainment can accelerate the impurities towards the plasma flow velocity, resulting in increased impurity-impact energies. In the companion paper [9], the impurities were found to be accelerated towards $M_{se} \approx 0.65$ of the common-system sound speed under ITER-like divertor plasma conditions, where M_{se} is the Mach number at the sheath edge. Therefore, the impurities had a considerably higher velocity than would be predicted from their thermal velocity, resulting in higher impurity-impact energies (figure 12). Therefore, the threshold energy for sputtering can be achieved at relatively low T_e, allowing for the erosion of W under low-temperature ($T_e < 5$ eV) plasma conditions. As the re-deposition rate strongly dropped with increasing E_i, sustaining a detached divertor will be crucial for achieving low E_i, and thereby low net erosion rates.

7. Conclusion

Pure Ar plasma exposures were performed in Magnum-PSI to study the erosion and re-deposition of W under high-density ($n_e > 2 \times 10^{20}$ m^{-3}), low-temperature ($T_e < 5$ eV) plasma conditions. These plasma conditions resulted in a regime in which entrainment became particularly important. The effect of entrainment on the ion-impact energy of impurities has been discussed in the companion paper [9]. In this work, we focus on the impact of entrainment on the erosion and re-deposition of W.

Considerable roughening of the W target's surface was found due to extensive sputtering by Ar bombardment. The μm-trenches and mass balance reveal that the erosion and re-deposition of W occured on the μm scale. High local re-deposition rates were found of up to 93%. These high local re-deposition rates show that neutral-ion interactions were important as the ionization length was long compared to the width of the target. The local re-deposition rate declined from $R \approx 93\%$ to $R \approx 68\%$ for increasing ion-impact energies from $E_i \approx 43$ eV to $E_i \approx 94$ eV. This trend can be coupled to the increasing energy of the sputtered W particles with E_i, hence increasing the number of collisions required to re-deposit the sputtered particle. The reduction in R with increasing E_i stresses the requirement for low-temperature divertor plasma conditions to keep the impurity impact energy low, especially considering the increase in impurity-impact energy by entrainment. In addition, a clear increase in re-deposition was found for higher plasma densities, which is linked to a reduction in both the entrainment and ionization length. Comparison experiments between PSI-2 and Magnum-PSI are foreseen to facilitate different n_e and T_e regimes, allowing for a deeper understanding of the plasma properties and the validation of plasma-wall interaction codes.

In the re-deposition profiles, a constant up-downstream asymmetry was found, revealing the occurrence of entrained re-deposition where sputtered W was dragged downstream by the plasma flow. In close vicinity to the W target, a left-right asymmetry was found, which was present at a smaller distance away from the surface with increasing ion-impact energies. Given the dominance of the up-downstream asymmetry in the re-deposition profile, entrained re-deposition was dominant over prompt re-deposition. This aligns with the characteristic length scales associated with both entrained and prompt re-deposition for the examined plasma conditions. Additionally, as the electron density increased, the re-deposition profile narrowed, consistent with the shortened mean free path of sputtered particles in denser plasmas. The re-deposited W appeared to be porous for which the grain boundaries of the underlying material are amplified. Further post-mortem

analysis of the re-deposited W is foreseen to characterize the layer properties in more detail.

The experimental results support the theoretical framework, which considers the friction between W impurities and the background plasma by ion–ion Coulomb collision and induced-dipole collisions for the ionized and neutral impurities, respectively. Although modeling will be required to extrapolate the Magnum-PSI results to ITER, the theoretical framework suggests re-deposition rates exceeding 99% for the highly collisional plasmas foreseen for ITER. While edge localized modes will promote prompt re-deposition, entrained re-deposition is expected to be dominant during the steady-state operation of ITER. Therefore, entrainment will play an important role in the erosion and re-deposition of plasma-facing materials in future fusion reactors.

Acknowledgments

We acknowledge the support of the Magnum-PSI Facility Team and the IBF team at DIFFER. The Magnum-PSI facility at DIFFER has been funded by the Netherlands Organisation for Scientific Research (NWO) and EURATOM. This work has been carried out within the framework of the EUROfusion Consortium, funded by the European Union via the Euratom Research and Training Programme (Grant Agreement No 101052200 - EUROfusion). Views and opinions expressed are however those of the author(s) only and do not necessarily reflect those of the European Union or the European Commission. Neither the European Union nor the European Commission can be held responsible for them. Work has been partly performed under EUROfusion WPPWIE.

CRediT authorship contribution statement

M.J.H. Cornelissen: Conceptualization, Methodology, Formal analysis, Investigation, Writing—Original Draft. **B. Tyburska-Pueschel:** Formal analysis, Supervision, Writing—Review & Editing. **M. Rasinski:** Investigation, Writing—Review & Editing. **S. Brons:** Methodology. **E. Zoethout** Investigation, Writing—Review & Editing. **D. Dorow-Gerspach:** Investigation, Writing—Review & Editing. **M. Wirtz:** Resources. **G. Pintsuk:** Resources. **S. Brezinsek:** Conceptualization, Writing—Review & Editing. **J. Beckers:** Supervision, Writing—Review & Editing. **T.W. Morgan:** Conceptualization, Supervision, Writing—Review & Editing.

ORCID iDs

Mark J.H. Cornelissen https://orcid.org/0000-0001-7576-4628
Beata Tyburska-Pueschel https://orcid.org/0000-0002-8434-5131
Marcin Rasinski https://orcid.org/0000-0001-6277-4421
Erwin Zoethout https://orcid.org/0000-0002-9012-6859
Daniel Dorow-Gerspach https://orcid.org/0000-0002-7149-0284
Sebastijan Brezinsek https://orcid.org/0000-0002-7213-3326
Marius Wirtz https://orcid.org/0000-0002-1857-688X
Gerald Pintsuk https://orcid.org/0000-0001-5552-5427
Job Beckers https://orcid.org/0000-0001-6116-7013
Thomas W. Morgan https://orcid.org/0000-0002-5066-015X

References

[1] Pitts R.A. *et al* 2013 A full tungsten divertor for ITER: physics issues and design status *J. Nucl. Mater.* **438** S48–S56
[2] Pütterich T., Fable E., Dux R., O'Mullane M., Neu R. and Siccinio M. 2019 Determination of the tolerable impurity concentrations in a fusion reactor using a consistent set of cooling factors *Nucl. Fusion* **59** 056013
[3] Krat S., Gasparyan Y., Vasina Y., Davletiyarova A. and Pisarev A. 2018 Tungsten-deuterium co-deposition: experiment and analytical description *Vacuum* **149** 23–28
[4] Loarte A. *et al* (the ITPA Scrape-off Layer and Divertor Physics Topical Group) 2007 Chapter 4: power and particle control *Nucl. Fusion* **47** S203
[5] Pitts R.A. *et al* 2019 Physics basis for the first ITER tungsten divertor *Nucl. Mater. Energy* **20** 100696
[6] Xiang L., Militello F., Moulton D., Subba F., Aho-Mantila L., Coster D., Wensing M., Lunt T., Wischmeier M. and Reimerdes H. 2021 The operational space for divertor power exhaust in DEMO with a Super-X divertor *Nucl. Fusion* **61** 076007
[7] van Swaaij G.A., Kirschner A., Borodin D., Goedheer W.J., Bystrov K. and De Temmerman G. 2014 Erosion/re-deposition modeling in an ITER divertor-like high-density, low-temperature plasma beam *Plasma Phys. Control. Fusion* **56** 095028
[8] van den Berg-Stolp J., van der Meiden H.J., Classen I.G.J., Vernimmen J.W.M., Li Y., Scholten J., Brons S. and van Rooij G.J. 2021 Thermalized collisional pre-sheath detected in dense plasma with coherent and incoherent Thomson scattering *Nucl. Fusion* **61** 096007
[9] Cornelissen M.J.H., Vernimmen J.W.M., Verstappen D.E., Zoethout E., Classen I.G.J., Beckers J. and Morgan T.W. 2025 Erosion enhancement by impurity entrainment in the highly collisional plasmas of Magnum-PSI *Nucl. Fusion* **65** 026009
[10] Guterl J., Bykov I., Ding R. and Snyder P. 2021 On the prediction and monitoring of tungsten prompt redeposition in tokamak divertors *Nucl. Mater. Energy* **27** 100948
[11] Brezinsek S. *et al* (JET Contributors) 2019 Erosion, screening and migration of tungsten in the JET divertor *Nucl. Fusion* **59** 096035
[12] Mayer M. *et al* (ASDEX-Upgrade Team) 2009 Tungsten erosion and redeposition in the all-tungsten divertor of ASDEX Upgrade *Phys. Scr.* **2009** 014039
[13] Hakola A., Koivuranta S., Likonen J., Herrmann A., Maier H., Mayer M., Neu R. and Rohde V. 2015 Erosion of tungsten and steel in the main chamber of ASDEX Upgrade *J. Nucl. Mater.* **463** 162–5
[14] Zamperini S., Donovan D., Unterberg E., Stangeby P., Nichols J., Duran J., Elder D., Neff A., Rudakov D. and Zach M. 2019 Transport of tungsten to collector probes in DIII-D *Nucl. Mater. Energy* **18** 87–92
[15] Kirschner A., Tskhakaya D., Kawamura G., Borodin D., Brezinsek S., Ding R., Linsmeier C. and Romazanov J. 2016 Modelling of impurity transport and plasma-wall interaction in fusion devices with the ERO code: basics of the code and examples of application *Contrib. Plasma Phys.* **56** 07

[16] van de Pol M.J. *et al* 2018 Operational characteristics of the superconducting high flux plasma generator Magnum-PSI *Fusion Eng. Des.* **136** 597–601
[17] van Eck H.J.N. *et al* 2019 High-fluence and high-flux performance characteristics of the superconducting Magnum-PSI linear plasma facility *Fusion Eng. Des.* **142** 26–32
[18] Park J.-S., Bonnin X., Pitts R. and Lore J. 2024 Impact of gas injection location and divertor surface material on ITER fusion power operation phase divertor performance assessed with SOLPS-ITER* *Nucl. Fusion* **64** 036002
[19] Dux R., Janzer A. and Pütterich T. (ASDEX Upgrade Team) 2011 Main chamber sources and edge transport of tungsten in H-mode plasmas at ASDEX Upgrade *Nucl. Fusion* **51** 053002
[20] Chankin A.V., Coster D.P. and Dux R. 2014 Monte Carlo simulations of tungsten redeposition at the divertor target *Plasma Phys. Control. Fusion* **56** 025003
[21] Sytova E., Kaveeva E., Rozhansky V., Senichenkov I., Voskoboynikov S., Coster D., Bonnin X. and Pitts R.A. 2018 Impact of a new general form of friction and thermal forces on SOLPS-ITER modelling results *Contrib. Plasma Phys.* **58** 622–8
[22] Chandra R., Akkermans G.R.A., Classen I.G.J., Perillo R., de Blank H.J., Diomede P. and Westerhof E. 2018 Numerical modelling of detached plasma experiments with differential pumping in Magnum-PSI *45th EPS Conf. on Plasma Physics,* (*Prague*, *2–6 July*), ed J. Berndt, S. Coda, G. Lapenta, C. Michaut, S. Weber and M. Mantsinen (European Physical Society (EPS)) P1.1030 (available at: https://indico.ipp.cas.cz/event/13/contributions/720)
[23] Summers H.P. 2004 *The ADAS User Manual* version 2.6 (available at: http://www.adas.ac.uk)
[24] Hutchinson I.H. 2002 *Principles of Plasma Diagnostics* 2nd edn (Cambridge University Press) (https://doi.org/10.1017/CBO9780511613630)
[25] Eckstein W. 2002 *Calculated Sputtering, Reflection and Range Values* IPP 9/132 Max-Planck-Institut für Plasmaphysik
[26] Viezzer E. *et al* 2023 Prospects of core-edge integrated no-ELM and small-ELM scenarios for future fusion devices *Nucl. Mater. Energy* **34** 101308
[27] Meiden H.J. *et al* 2012 Advanced Thomson scattering system for high-flux linear plasma generator *Rev. Sci. Instrum.* **83** 123505–1/12
[28] Mayer M. 2020 *SIMNRA User's Guide* version 7.03 Technical Report Max-Planck-Institut für Plasmaphysik
[29] Morgan T.W., Balden M., Schwarz-Selinger T., Li Y., Loewenhoff T.H., Wirtz M., Brezinsek S. and De Temmerman G. 2020 ITER monoblock performance under lifetime loading conditions in Magnum-PSI *Phys. Scr.* **2020(T171)** 014065
[30] Kuhn S., Riemann K.-U., Jelić N., Tskhakaya D.D., Tskhakaya D. and Stanojević M. 2006 Link between fluid and kinetic parameters near the plasma boundary *Phys. Plasmas* **13** 013503
[31] Behrisch R. and Eckstein W. 2007 *Sputtering by Particle Bombardment* (Springer)
[32] Cupak C. *et al* 2021 Sputter yields of rough surfaces: importance of the mean surface inclination angle from nano- to microscopic rough regimes *Appl. Surf. Sci.* **570** 151204
[33] Marenkov E., Nordlund K., Sorokin I., Eksaeva A., Gutorov K., Jussila J., Granberg F. and Borodin D. 2017 Angular and velocity distributions of tungsten sputtered by low energy argon ions *J. Nucl. Mater.* **496** 18–23
[34] Nichols J.H. *et al* 2021 Modeling of E×B effects on tungsten re-deposition and transport in the DIII-D divertor *Nucl. Fusion* **61** 096018
[35] Wang H. *et al* 2024 Drifts effect on the divertor W leakage mechanisms under different dissipative divertor conditions of EAST *Nucl. Fusion* **64** 046009